Engineering Structures 335 (2025) 120211

Contents lists available at ScienceDirect

Engineering Structures

journal homepage: www.elsevier.com/locate/engstruct

Seismic steel frames enhanced with locally resonant metastructures for reduced embodied carbon

Jiawei Zhang [a,b], Tugberk Guner [b], Oreste S. Bursi [b],*, Zheng Lu [a,c],**

[a] Department of Disaster Mitigation for Structures, Tongji University, Shanghai, 200092, China
[b] Department of Civil, Environmental and Mechanical Engineering, University of Trento, Trento, 38123, Italy
[c] State Key Laboratory of Disaster Reduction in Civil Engineering, Tongji University, Shanghai, 200092, China

ARTICLE INFO

Keywords:
Locally resonant metastructures
Controlled moment resisting steel frame
Controlled eccentrically braced steel frame
Mass reduction
Carbon emission quantification

ABSTRACT

This paper introduces controlled steel buildings endowed with novel locally resonant metastructures inspired by metamaterial concepts. A major limitation of finite locally resonant metastructures in low-frequency vibration control is the requirement for large additional masses. Conversely, properly designed periodic structures inside a main structure can function as locally resonant metastructures with limited extra mass and proper damping. By incorporating locally resonant metamaterials, this study advances the potential of seismic steel frames, to enhance seismic performance while reducing material usage, thus addressing both structural efficiency and sustainability. Therefore, our research covers both the elastic and the inelastic range, where frames are optimally designed to meet both immediate occupancy and life safety performance limit states. In addition, two case studies, one involving a 25-story moment resisting steel frame and the other focusing on a 20-story eccentrically braced steel frame structure, are analyzed to demonstrate the efficacy of the proposed approach. A multi-objective optimization methodology is employed to illustrate the trade-off between metastructure inherent damping ratio and material usage, i.e. embodied carbon emissions, highlighting the environmental benefits alongside structural performance improvements. The results demonstrated that optimal mass reduction for the proposed metastructures in both lateral-resisting systems was feasible, with reduction rates of at least 11.3% and 13.7% without additional damping in the metastructures compared to the original configurations. Finally, the reduction in embodied carbon was analyzed based on the material usage in the framed structures.

1. Introduction

1.1. Background and motivations

The impact of the construction sector on energy consumption and the environment has been a major concern. In 2021, the construction sector accounted for 37% of worldwide carbon emissions and 36% of the global primary energy supply [1]. In particular, the building sector is responsible for 35% of the EU's total waste generation, and material efficiency has played an important role in reducing greenhouse gas (GHG) emissions [2]. Furthermore, in 2018, 835 million tons of steel and its products were produced in China, representing 48.8% of the total world, leading to 11% of the Chinese energy consumption [3].

Carbon emissions occur throughout the life cycle of a building – from the extraction of materials to the end-of-life phase – while the transition between these phases generates substantial transportation-related emissions, adding to the life cycle carbon footprint (LCCF) of buildings [4,5]. Carbon emissions are generally classified into two categories: embodied carbon and operational carbon emissions [6]. Embodied carbon generally refers to emissions generated during the initial stages of the building's life cycle, such as material extraction, processing, conceptual design, detailed design and construction. A significant step in reducing embodied carbon is the efficient use of appropriate materials in the structural system, particularly during the conceptual design phase; it has, indeed, the greatest impact on both costs and environmental effects, accounting for 70% to 80% of the resources utilized in a project [7]. Therefore, considerable effort is ongoing to provide frameworks that choose adequate reliability levels not only in terms of monetary optimization and societal risk acceptance with respect to life safety but also to objectives related to environmental sustainability (risk-informed approaches). This should translate into a desired optimal balance between structure-inherent safety levels and resources allocated to that end. See, in this respect, the optimization carried out

---

* Corresponding author.
** Corresponding author at: Department of Disaster Mitigation for Structures, Tongji University, Shanghai, 200092, China.
E-mail addresses: oreste.bursi@unitn.it (O.S. Bursi), luzheng111@tongji.edu.cn (Z. Lu).

https://doi.org/10.1016/j.engstruct.2025.120211
Received 19 November 2024; Received in revised form 25 February 2025; Accepted 25 March 2025

by Hingorani and Kohler [8] on steel beams in buildings subjected to vertical loads, that achieved reductions in costs and materials at the design stage up to approximately 10%. Moreover, to identify the most suitable steel lateral resisting system with specific materials and configurations capable of reducing embodied carbon, Kanyilmaz et al. showed the possibility of selecting appropriate materials and structural system at the conceptual design stage based on the multi-objective genetic algorithm based on the non-dominated sorting genetic optimization algorithm (NSGA-II) [9–11]. However, alongside design optimization for embodied carbon reduction, concrete and steel quantities reduction can lead to a decrease in lateral stiffness and reliability, resulting in increased deformability. Therefore, for structures located in disaster-prone areas, such as those that frequently experience earthquakes, a trade-off must be found between structure-inherent safety and carbon emission reduction [12].

At the same time, studies on modern performance-based seismic design emphasize the importance of achieving performance objectives. In particular, performance-based seismic design has gained an increased prominence in earthquake resistant building design, where performance objectives are classified based on multi-hazard levels and lateral resisting systems [13]. Therefore, several studies cover optimal seismic design and sustainability by combining seismic performance and environmental impact analysis [14–16]. In particular, several seismic protection techniques have been investigated to improve seismic performance while preserving the original structural configurations, such as local joint strengthening methods [17,18], additional lateral load-resisting systems [19], and supplemental damping systems [20, 21]. More specifically, supplemental damping systems, like tuned mass dampers (TMDs), can be considered during the initial conceptual design stage and have proven efficient in practical engineering. However, they require a relatively large mass ratio, greater than 12%, to achieve a wide-frequency-range vibration control. Multiple tuned mass damper (MTMD) systems, where TMDs can be vertically distributed on the building based on modal analysis, have been proposed to mitigate multi-modal vibrations [22].

With effective elastic wave attenuation capabilities in specific frequency ranges, the so called band gaps, metamaterials and metastructures have garnered growing interest in vibration control. More specifically, metastructures, composed of a finite number of units due to their size, present a promising wave manipulation behavior through their overall geometry, dimensions, and boundary conditions. Locally resonant metastructures, which can achieve a low frequency band gap due to the local resonance of the internal units, provide an efficient solution for seismic protection. For instance, to manipulate seismic surface Rayleigh waves, Chen et al. [23] proposed an LRM-based metaconcrete, where classic aggregates were replaced by locally resonant ones with a soft rubber coating. Hao et al. [24] proposed a novel LRM design with the soft-material intermediate layer inside a punched thin plate to mitigate low-frequency vibration. To protect large process equipment subjected to seismic loading, periodic foundations have been suggested to function as base isolation systems. In particular, locally resonant metafoundations, were developed by Bursi and co-workers [25], for wave manipulation in the low-frequency range. The metafoundation, composed of heavy reinforced concrete resonator blocks attached to the foundation slab by means of wire ropes, requires additional mass to be implemented to protect the superstructure. Moreover, their seismic mitigation performances were further experimentally investigated by Xiao et al. [26]. And to a greater extent, Guner et al. [27] introduced metafoundations for the seismic protection of a Small Modular Reactor (SMR) nuclear power plant subjected to both horizontal and vertical excitations.

Nonetheless, limited research has explored the application of metastructures inside conventional buildings. One of the reasons is the possible addition of inertia in upper stories; another issue is the lack of space to allocate relative large resonators. Clearly, the width of the frequency band gap is limited by the mass ratio of the resonant unit to the modal mass. Some methods exploiting nonlinearities have also considered amplifying the resonant unit capabilities. Xia et al. [28] introduced bistable resonators to enhance frequency bandwidth of the band-gap. Zhao et al. [29] proposed a nonlinear metastructure with bi-linear oscillators for broadband vibration suppression. Kalderon et al. [30] introduced a mass amplification mechanism using a hinged, rigid rod. Additionally, studies on multi-stable columns [31], inerter-enhanced metamaterials [32], and quasi-periodic configurations [33] have been conducted. Nonetheless, it remains challenging to widen the frequency range where elastic waves cannot propagate in a building due to severe constraints.

1.2. Scope and core contribution

In sum, to enhance the seismic performance of typical steel buildings with specific materials and configurations capable of reducing embodied carbon, the following objectives are pursued hereinafter: (i) to conceive and design steel buildings as controlled systems by means of optimized locally resonant metastructures (LRMs) that filter seismic waves via the dynamics (antiresonance) of local resonators; (ii) to optimize each entire building to decrease mass and control damping of metastructures, resulting in reduced embodied carbon emissions while also satisfying reliability requirements and performance-based seismic design (PBSD) objectives.

Therefore, guided by the wave methods used in metamaterials, specific LRM layouts are proposed in this paper. The building structures composed of moment resisting or braced steel frames are designed with coupled vertically distributed internal metastructures. The wave dispersion and transmissibility properties of the finite periodic structure are analyzed. In this study, one major contribution is the integration of LRMs within steel frame structures, demonstrating their ability to enhance seismic performance while reducing material usage and also embodied carbon emissions. Another key focus is the investigation of the seismic performance of metastructures-coupled steel frames, since to ensure robustness under realistic seismic conditions, particular attention is given to their behavior in the nonlinear regime. Additionally, a multi-objective optimization framework is developed to balance damping properties and material efficiency, providing a sustainable and efficient design methodology that aligns structural performance with environmental goals. These contributions are further validated through nonlinear time–history analyses with respect to (w.r.t.) basic performance objectives, i.e., life safety (LS) and immediate occupancy (IO). Clearly, at the LS limit state, the examined frames experience inelasticity, which is properly taken into account during the optimization procedures.

The aforementioned procedure was applied to two different case studies: (i) a 25-story moment resisting steel frame; (ii) a 20-story eccentrically braced steel frame. Each building has been designed based on relevant standards according to their construction site. Then, a multi-objective optimization algorithm has been applied to achieve material savings with increasing damping ratios of the metastructures. The rest of the paper is organized as follows. The fundamental concept of LRMs, modeling and band gap formation properties are presented in Section 2. Section 3 outlines the design and optimization procedures, according to the aforementioned methodology. Section 4 instead presents the optimization results for the two case studies endowed with LRMs. Life cycle assessment and reduction in embodied carbon emissions are assessed in Section 5. Finally, conclusions and future perspectives are drawn in Section 6.

2. Metastructures for steel frames

This section introduces the methodology of the frame structure coupled with locally resonant metastructure approach and explains its fundamental dynamic mechanism. The proposed metastructure-based design approach is illustrated on an ideal shear frame with three bays,

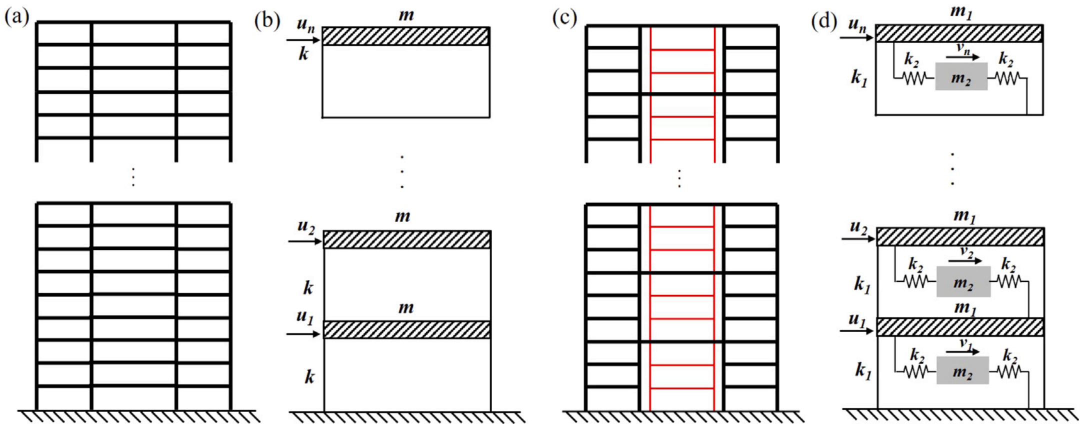

Fig. 1. Simple shear-type frame: (a) the uncontrolled frame structure; (b) condensed model of the original frame; (c) metastructure-coupled frame; (d) condensed model of the coupled frame. (For interpretation of the references to color in this figure legend, the reader is referred to the web version of this article.)

as indicated in Fig. 1(a) and (b). Accordingly, the proposed controlled metastructure-coupled structure layout is presented in Fig. 1(c) and (d), where in the middle bay, beams were periodically detached from outer beams and new inner columns were introduced. In this configuration, the main structure, i.e. the outer two bays, marked in black, represent the primary lateral resisting system, while the detached inner middle-bay stories, marked in red, define the LRMs. Basically, in the LRMs, the slabs and their supporting beams, which are not connected to the outer frames in the horizontal direction, can move independently from the outer frames. The LRMs are designed to cope with the desired band gap properties; and the clearances between the columns of the LRMs and the outer frames are set to avoiding collisions between structural elements, e.g. floors and walls, under lateral displacements. In the proposed coupled – controlled – structure, the internal LRMs filter the greater part of vibrations from the outer frames in the band gap frequency range, and, in addition, dissipate energy through the inherent damping of the metastructures. While the proposed LRMs rely on resonance behavior for vibration control, similar to TMD systems, they differ in their integration with the structure as periodic metastructures. This integration enables the formation of bandgaps that suppress vibrations across a range of frequencies, similar to the choral effect of multiple TMDs. Conversely, TMDs are typically designed to target a specific resonance frequency, and require additional mass and associated costs. If one considers the seismic waves traveling through the frame, the outer frames can be analogously replaced with a shear-type system, as depicted in Fig. 1(b). Accordingly, as the seismic wave propagate from foundation to the upper stories, the inherent damping in the frame – not drawn for simplicity – dissipates wave energy. In the case of metastructures and using the similar analogy, periodic spring–mass systems can be drawn as in Fig. 1(d). The LRMs approach clearly resembles the MTMD approach; nonetheless, the proposed system also benefits from the so-called metadamping effect provided by the (finite) periodicity of the LRMs [34]. To clarify this phenomenon, an analytical treatment on the frame to hand is carried out herein, excluding physical damping.

The masses of the outer frames and metastructures are denoted by m_1 and m_2, respectively, with the corresponding lateral stiffness values k_1 and k_2. For the jth degree of freedom in the outer frames subjected to the sinusoidal excitation $\ddot{x}_g$, the governing system of equations of motion can be expressed as follows:

$$\begin{cases} m_1\ddot{u}_j + k_1(2u_j - u_{j-1} - u_{j+1}) + k_2(2u_j - v_j - v_{j+1}) = -m_1\ddot{x}_g \\ m_2\ddot{v}_j + k_2(2v_j - u_j - u_{j-1}) = -m_2\ddot{x}_g \end{cases} \tag{1}$$

with $\omega_2 = \sqrt{k_2/m_2}$. The internal metastructure displacement, v_j can be solved by Eq. (1).

$$v_j + v_{j+1} = \frac{\omega_2^2}{2\omega_2^2 - \omega^2}(2u_j + u_{j+1} + u_{j-1}) + \frac{2\omega^2}{2\omega_2^2 - \omega^2}x_g \tag{2}$$

where ω is the input excitation frequency and x_g is the corresponding amplitude. By substituting (2) into (1) one obtains,

$$-\omega^2\left(1 + \frac{2k_2}{m_1(2\omega_2^2 - \omega^2)}\right)[\mathbf{M}]\mathbf{U} + \left(1 + \frac{\omega_2^2 k_2}{k_1(2\omega_2^2 - \omega^2)}\right)[\mathbf{K}]\mathbf{U} = \left(\omega^2 + \frac{2\omega^2 k_2}{m_1(2\omega_2^2 - \omega^2)}\right)[\mathbf{M}]x_g \tag{3}$$

where $[\mathbf{M}]$ and $[\mathbf{K}]$ define the mass matrix and stiffness matrices of the outer frames, respectively. $\mathbf{U} = [u_1, u_2, \ldots, u_n]^T$ is the displacement vector of them, which can be expressed as the superposition of modes $U = \sum \phi_j Y_j$, $\boldsymbol{\Phi} = \{\phi_j\}$ and Y_j are the mode shapes and amplitudes. The orthogonality condition of the modes entails that:

$$\begin{cases} \{\phi_j\}^T[\mathbf{M}]\{\phi_i\} = 0 & \text{if } i \neq j \\ \{\phi_j\}^T[\mathbf{M}]\{\phi_i\} = 1 & \text{if } i = j \end{cases} \tag{4}$$

$$\begin{cases} \{\phi_j\}^T[\mathbf{K}]\{\phi_i\} = 0 & \text{if } i \neq j \\ \{\phi_j\}^T[\mathbf{K}]\{\phi_i\} = \omega_j^2 & \text{if } i = j \end{cases} \tag{5}$$

Substituting (4) and (5) into (3), for the jth mode of the outer structure, where j is arbitrary:

$$\left[-\omega^2\left(1 + \frac{2k_2}{m_1(2\omega_2^2 - \omega^2)}\right) + \omega_j^2\left(1 + \frac{\omega_2^2 k_2}{k_1(2\omega_2^2 - \omega^2)}\right)\right]Y_j = F_j \tag{6}$$

$$F_j = \{\phi_j\}^T\left(\omega^2 + \frac{2\omega^2 k_2}{m_1(2\omega_2^2 - \omega^2)}\right)m_1 x_g \tag{7}$$

where ω_j is the jth frequency. Therefore, Eq. (6) can be solved for Y_j in a closed-form expression:

$$Y_j = \frac{F_j}{-\omega^2\left(1 + \frac{2k_2}{m_1(2\omega_2^2 - \omega^2)}\right) + \omega_j^2\left(1 + \frac{\omega_2^2 k_2}{k_1(2\omega_2^2 - \omega^2)}\right)} \tag{8}$$

The input excitation frequencies match the modal frequencies of the whole frame structure when the amplitudes Y_j is infinite. Therefore, internal metastructure resonance result in two additional resonant peaks on both sides of their own uniform natural frequency, which can be determined by solving the positive roots of the denominator in (8). They read,

$$\begin{cases} \omega^+ = \sqrt{(\sigma + 2k_1k_2m_1 + 2k_1k_2m_2 + k_1m_1m_2\omega_j^2)/(2k_1m_1m_2)} \\ \omega^- = \sqrt{(-\sigma + 2k_1k_2m_1 + 2k_1k_2m_2 + k_1m_1m_2\omega_j^2)/(2k_1m_1m_2)} \end{cases} \tag{9}$$

where, (see Eq. (10) in Box I).

The additional frequencies ω^+ and ω^- arise from the splitting of the original resonant frequency of the outer frame, induced by the resonance of the metastructures. When the modal frequency of the

$$\sigma = \sqrt{k_1\left(-4k_2^2m_1^2m_2\omega_j^2 + 4k_1k_2^2m_1^2 + 8k_1k_2^2m_1m_2 + 4k_1k_2^2m_2^2 - 4k_1k_2m_1^2m_2\omega_j^2 + 4k_1k_2m_1m_2^2\omega_j^2 + k_1m_1^2m_2^2\omega_j^4\right)} \tag{10}$$

Box I.

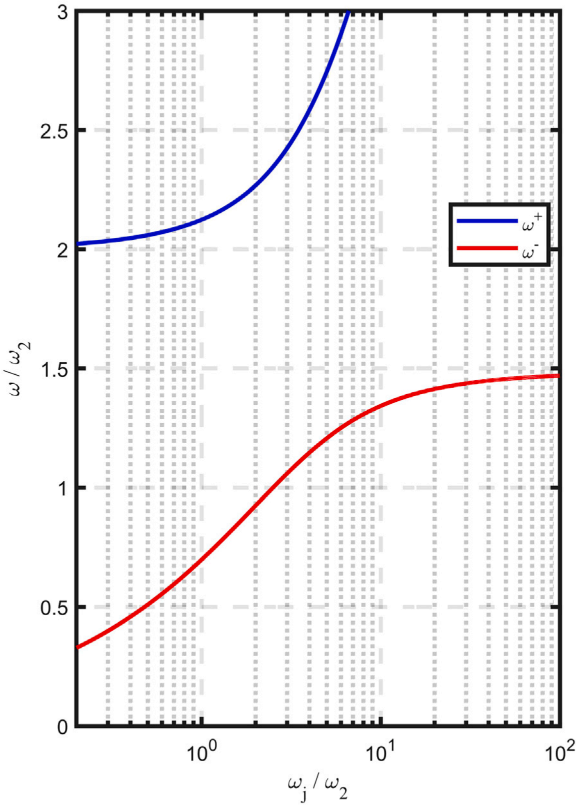

Fig. 2. Input excitation frequency as a function of coupled structural resonant frequencies.

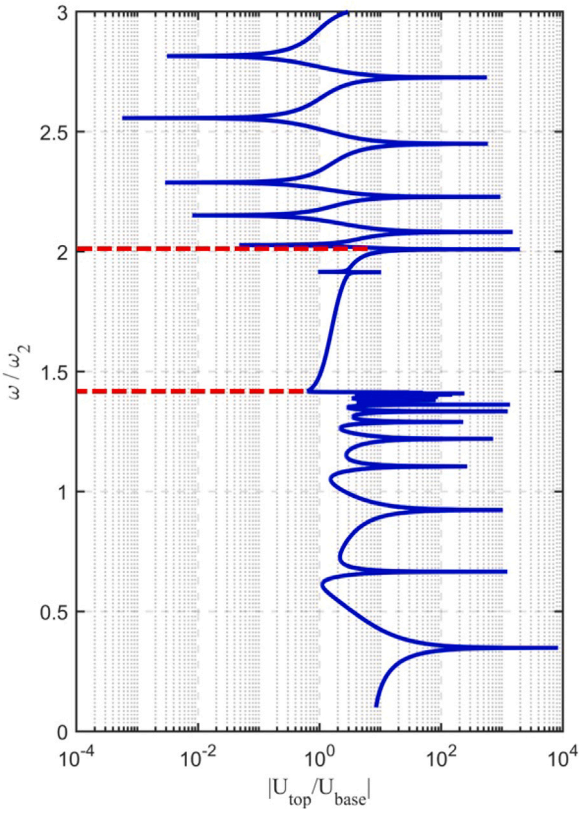

Fig. 3. Input excitation frequency as a function of wave transmissibility.

outer frame approaches its extreme values of 0 and infinity, a frequency range emerges where no additional resonance peaks are present, forming a band gap. The metastructure-induced resonant frequencies in the coupled structure are shown in Fig. 2, under varying modal frequencies of the coupled structure. The mass ratio $\mu = m_2/m_1$ and stiffness ratio $\gamma = k_2/k_1$ are considered to be 1 and 0.2, respectively. The transmissibility, defined as the displacement amplitude ratio of the top story to the first story, is examined for 15 periodic unit cells when the structure is excited by a sinusoidal wave, as shown in Fig. 3. The results indicate that the finite system can effectively suppress vibrations when the excitation frequency falls within the band gap. For clarity, the band gap limits computed in Eq. (9) are marked by two dashed red lines.

The proposed coupled structure endowed with the LRMs, can mitigate unfavorable vibrations within the band gap without the need for additional masses as in the case of MTMDs or additional damping systems. Therefore, the subsequent sections aim to achieve coupled structural configurations endowed with reduced material use and the same seismic performance objectives. This goal will of course reduce construction costs and LCFF.

3. Structural design and optimization framework

In the proposed coupled frame structure, metastructures vibrate out-of-phase w.r.t. the outer frame due to local antiresonance effects. Therefore, the inherent damping of metastructures can be optimized to enhance the overall seismic performance of the coupled structure, while limiting the interstory drifts through the use of additional damping devices [35]. Given the different level of damping between the metastructures and the outer frame, the damping of the metastructures has been considered as an equivalent non-proportional damping [36] and is applied to the coupled structure through a finite element (FE) analysis in the OpenSEES software [37].

3.1. Optimization procedure

Taking into account both the seismic performance and the LCCF of the proposed coupled structure layout, a design procedure combined with optimization has been developed to minimize material usage. The process ensures the compliance with the performance objectives, i.e. interstory drift ratio requirement, δ, in accordance with the PBSD methodology. The workflow for the optimization and section design procedure is shown in Fig. 4. To achieve the minimization of structural weight of both the outer frame and the metastructure, in parallel with the optimal metastructure damping ratio, the NSGA-II was employed [11].

During the optimization, damping ratios up to 20% were considered. For steel structures, a minimum of 2% damping, attributed to internal friction and energy dissipation at connections, was assumed.

In moment resisting metastructures, higher damping ratios can be achieved using damping systems. For smaller damping requirements, friction-based beam–column joints can be employed [38], while additional viscous dampers are necessary for higher damping levels [39]. In braced metastructures, the design of the links can be modified to meet specific damping requirements [40], with viscous or hydraulic dampers added as needed to achieve higher ratios.

For the optimization process, the floor plans and material use of the original structure and coupled structure are fixed. Therefore, only the sections in each bay of the coupled structure and metastructure inherent damping ratio are considered as variable in the optimization. As sketched in Fig. 4, the variables are randomly generated as a parent population in the initial generation, where the sections are encoded from a predefined section library. The combination of the generated sections and the metastructure damping ratio forms a conceptual design of the proposed structure. Unlike the traditional GA optimization algorithm, a mapping from the generated sections to stress-passed sections is established through a section design procedure, where each element must meet the requirements with a minimum section area in an iterative design process, according to the corresponding standards.

Nonlinear time–history analyses were conducted with the OpenSEES software [37], to determine the maximum interstory drift ratio (IDR) δ_{max} for both life safety (LS) and immediate occupancy (IO) safety objectives, according to the standard FEMA 356 [13]. In the optimization process, the structural model was constructed using “Fiber” sections within the “nonlinearBeamColumn” elements. The H-type sections were modeled using the “WFSection2D” section, with four fibers in the web and each flange, respectively. The box sections were discretized with ten fibers per quadrilateral. In addition, the integration along each element employed the Gauss–Lobatto quadrature rule with five integration points. This approach allows for an accurate distributed-plasticity representation of yielding. The material properties were defined using the “Steel02” material model, with a strain-hardening ratio (the ratio between the post-yield tangent and the initial elastic tangent) set to 0.01. The parameters for the steel hysteretic constitutive law were suggested and validated based on prior research [41–43], and the favorable behavior of the FE software in the nonlinear regime was demonstrated through an experimental real-time hybrid simulation of a steel frame structure [44]. Moreover, sensitivity results from the case studies analyzed in depth in Section 4, performed with refined meshes in the most unfavorable situation, i.e. with $\xi_{meta} = 0.02$, clearly indicate that structural responses are independent of mesh refinement, thus demonstrating the accuracy of the assumed FE models in the optimization process.

Each structural solution during the NSGA-II run was subjected to three natural ground motion records, which were selected based on the design spectrum with return periods of 475 and 72 years, for the LS and IO states, respectively. In the optimization process, the maximum structural IDRs, evaluated based on two safety limit states, had to remain below the threshold values specified by FEMA 356 standards. In addition, to guide the algorithm in selecting elite individuals for a lightweight optimal structural design, while ensuring comparable structural performance across different damping ratios, a supplementary condition was imposed for the LS limit state. Specifically, the ratio δ_{LSmax} was required to exceed 80% of the limit value $\delta_{LSlimit}$, ensuring that the overall performance remains unaffected. When the time-history results did not satisfy the aforementioned condition, a penalty multiplier was applied to the multi-objective fitness. The penalty multiplier penalizes designs that fail to meet performance thresholds, specifically interstory drift limits in the IO and LS limit states. In such cases, the total frame mass is multiplied by a factor of 10^6, thus ensuring that the optimization process prioritizes safety-compliant solutions and effectively accelerates convergence by discouraging infeasible designs early in the optimization process.

After evaluating the fitness functions with the penalty, a step involving the execution of genetic operators, including “selection”, “crossover”, and “mutation”, has been applied to produce the best offspring population in that generation. The termination criterion for each generation checks whether all elite individuals in the current generation are identical to those in the previous generation or if the generation count reaches the preset maximum value. For a fair comparison, the original uncontrolled structures with conventional layout was also optimized following the same above-mentioned procedure. The multi-objective optimization procedure was implemented in the MATLAB software. An intermediate crossover method with a crossover fraction of 0.8 was employed, and the Pareto fraction was set to 0.35.

3.2. Site-specific seismic hazard and accelerograms selection

For purposes of generality, two configurations of coupled structures have been examined: a steel moment-resisting frame (MRF) and a steel eccentrically braced frame (EBF) structure, which have been assumed to be located in Melilli, Sicily, Italy and El Centro, California, USA, respectively. Therefore, the design response spectra corresponding to different performance objectives were determined according to the Italian standard NTC 2018 [45] and the USA standard ASCE 7-22 [46], respectively. In particular, the design spectra for IO and LS limit states have been selected with return periods of 72 years and 475 years, corresponding to 50% and 10% probabilities of exceedance over 50 years, respectively. As shown in Fig. 5, three spectrum-compatible accelerograms were selected to match the design spectrum around the fundamental period of the examined structures; it has been estimated by means of,

$$T_a = C_t h_n^x \tag{11}$$

according to ASCE 7-22, where the coefficients C_t and x can be determined based on the lateral system type, while h_n defines the total structural height.

In particular, the approximate fundamental periods for the MRF and EBF structure read 3.11 s and 1.82 s, respectively from Eq. (11).

With regard to the MRF structure built in Melilli, Italy, it was assumed that the site’s soil type and topography were classified as C and T2, respectively. Based on the approximate fundamental periods, accelerograms were selected from the database established by the Pacific Earthquake Engineering Research Center (PEER) to match the design spectrum in the period range of 3 to 6 s, as shown in Fig. 5(a) and (b). Conversely, for the EBF structure located in El Centro, USA, it was assumed that the structure was designed with risk category II and seismic design category D. Then, three accelerograms have been chosen to match the multi-period design spectra [46] in the range 0.5–3.0 s, as depicted in Fig. 5(c) and (d). With this choice, standards NTC 2018 [45] and FEMA 356 [13] require to operate with the most unfavorable responses provided by the analyses.

4. Case studies and weight reduction

To evaluate the weight reduction capabilities of the proposed LRMs based on the optimization procedure described in Section 3, two case studies with different steel systems for bearing lateral forces have been considered. For weight comparison, we recall that the original structure is defined as uncontrolled structure to be compared with the proposed coupled (controlled) structure. Hereinafter, the detailed configurations and optimization results for both the uncontrolled and controlled coupled structures are presented, and the relationship between weight reduction effects and metastructure damping ratios is analyzed, offering a reference for estimating embodied carbon reduction in Section 5.

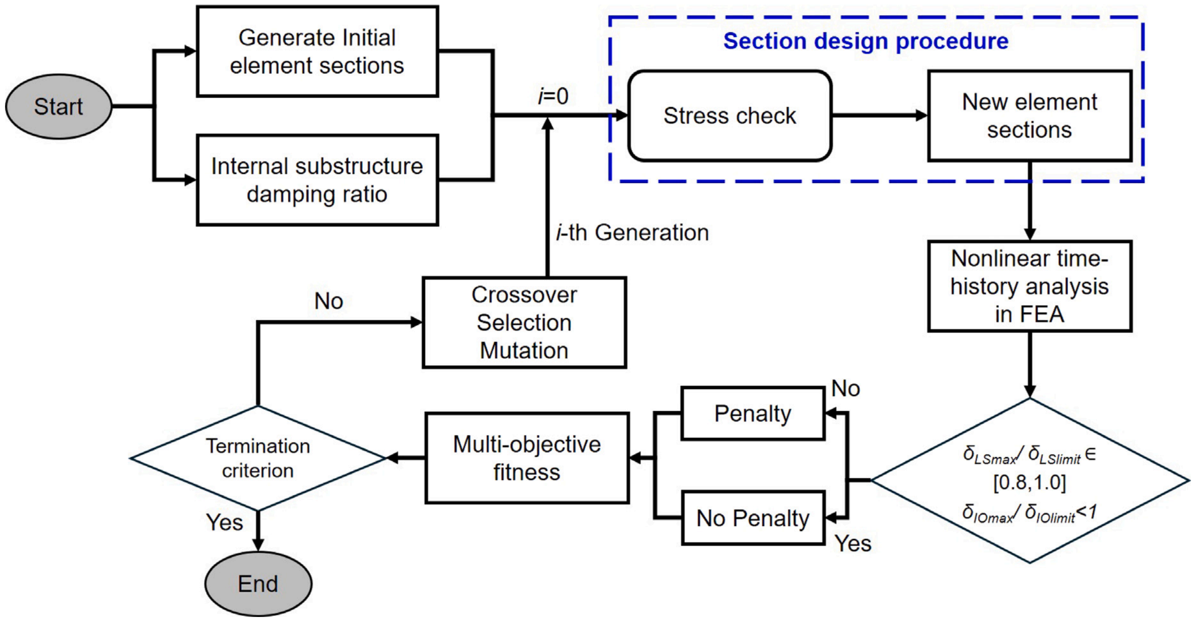

Fig. 4. Performance-based seismic design workflow for optimal weight reduction.

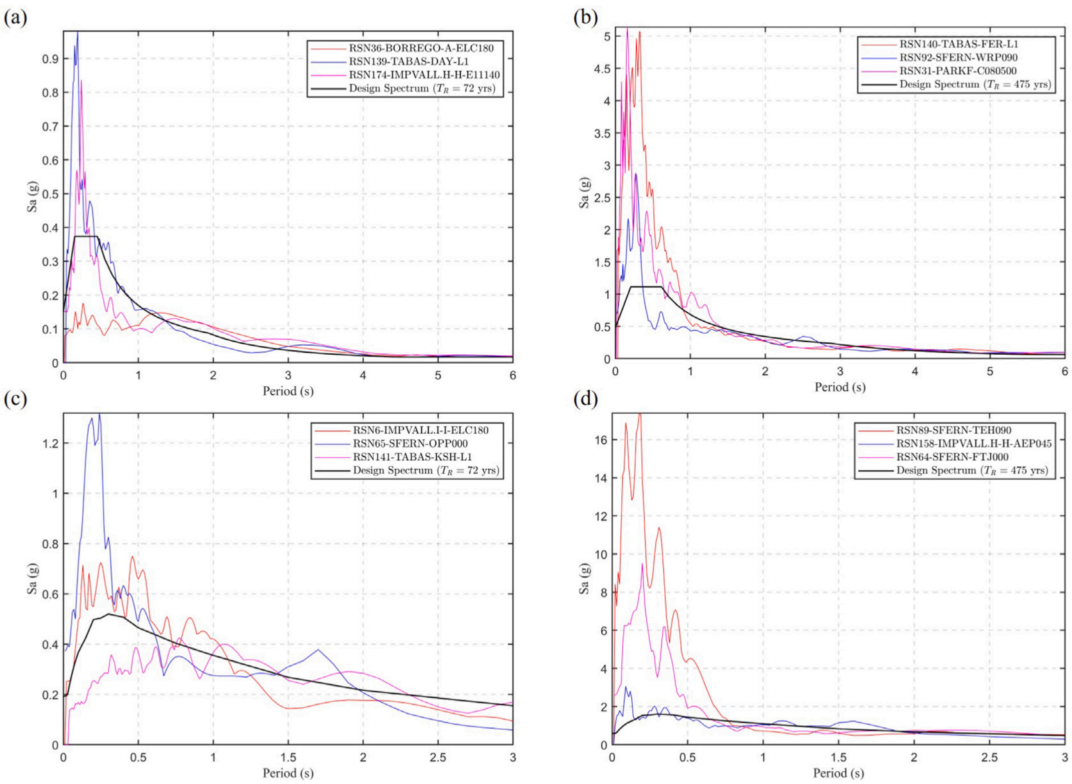

Fig. 5. Spectra of selected accelerograms and design spectra: (a) spectra for the IO limit state relevant to the MRF structure; (b) spectra for the LS limit state for the MRF structure; (c) spectra for the IO limit state for the EBF structure; (d) spectra for the LS limit state for the EBF structure.

4.1. Case study 1: a 25-story steel moment resisting frame

4.1.1. Building configuration

Based on building structure analyzed in [47], a 25-story steel moment resisting frame office building, with a vertically periodic distribution was selected as first example. It was assumed that the building was located in the Melilli, and the design was carried out in agreement with Eurocode 3 Part 1.1 [48] and Eurocode 8 Part 1. [49]. The floor plan and vertical plan of the uncontrolled structure is shown in Fig. 6, where the structure is composed of symmetric wide-flange beams and box section columns, with the maximum inertia oriented along the horizontal direction. The main structural parameters are collected in Table 1.

The 25-story MRF coupled structure shown in Fig. 7, keeps the same floor number of the original structure. Nonetheless, the outer frame columns remained continuously connected, while the part of the middle bays have been periodically modified. Five three-story locally resonant metastructures (LRMs), which are plotted in red in Fig. 7(a), are

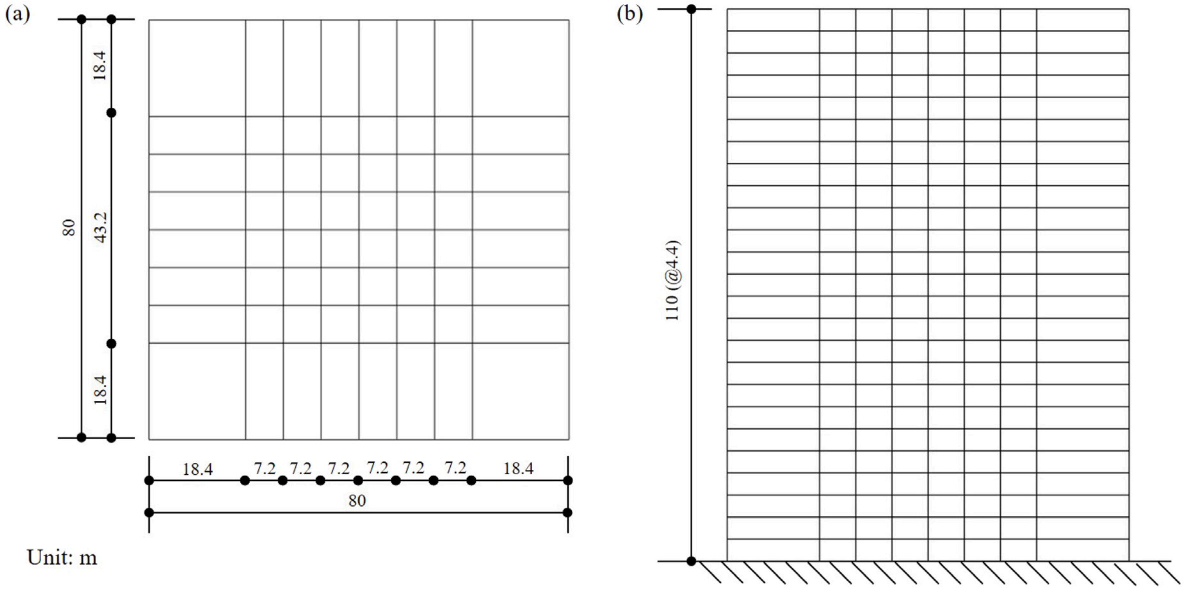

Fig. 6. Uncontrolled MRF structure: (a) Floor plan; (b) Lateral view.

Table 1
Main parameters of the MRF structure.

Outer bay length	18.4 m	Steel grade (S460)	f_{yk} = 460 MPa
Internal bay length	7.2 m	Superimposed linear dead load	5 kN/m^2
Number of stories	25		
Story height	4.4 m	Superimposed linear live load	2 kN/m^2

Table 2
Steel mass in the MRF structure with different ξ_{meta} values.

ξ_{meta}	Uncontrolled structure steel mass (t)	Coupled structure steel mass (t)	α
0.02	6111.6	5420.3	0.887
0.03		5180.3	0.848
0.05		5009.3	0.820
0.07		4857.7	0.795
0.11		4771.1	0.781
0.13		4771.0	0.781
0.17		4738.1	0.775
0.20		4704.0	0.771

distributed periodically along the height with the columns connected both at the top and at the bottom beam of the outer frame. All beam-to-column joints for both uncontrolled structure and coupled structure are assumed to be rigid joints. The uncontrolled structure as well as the outer frame in the coupled structure is designed with a 2.0% inherent damping ratio, while the inherent damping of internal metastructures can vary during the optimization process. The inner floor slabs of the metastructures, which are separated from the outer frame, can freely move as the periodic resonators sketched in Fig. 1. The details of the metastructures joints and outer frame are also shown in Fig. 7(b), where seismic expansion joints are set for the clearance between outer frame columns and metastructure side columns. According to Otsuki et al. [50], the length for floor and wall expansion joint can be set based on the inside slide between both sides for all three moving directions, while the design motion range was 175 mm. Therefore, in the case study, the relative displacement between metastructure columns and outer frame structure columns was also considered with an allowed clearance set to 175 mm.

4.1.2. Optimization results

In agreement with FEMA-356 [13], the limit values of the IDR corresponding to IO and LS performance objectives were considered as 0.7% and 2.5%, respectively. Clearly, the controlled structure layout did not change the concrete slab mass w.r.t the original layout of the uncontrolled structure; thus for optimization, only steel masses were reduced. Both the metastructure's equivalent damping ratio ξ_{meta} and the steel mass ratio α of the coupled structure to the uncontrolled structure have been set as objectives in the optimization. The Pareto front results are presented in Fig. 8 and Table 2, where the trade-off between steel mass ratio α and LRM damping ratio ξ_{meta} is evident. As detailed in Section 3.1, while comparable seismic performance was maintained during optimization, the trade-offs introduced can lead to variations in cost and environmental outcomes. Reducing steel weight decreases both material costs and embodied carbon, whereas incorporating damping systems can raise expenses. Achieving an optimal solution requires balancing total costs, environmental objectives, and seismic performance requirements.

The detailed optimized results for the metastructure and outer frame structure are provided in the Appendix. The monotonic pushover results, using the first mode shape as lateral force distribution, for the uncontrolled structure and coupled structures with varying metastructure inherent damping ratios are presented in Fig. 9. The uncontrolled structure, characterized by greater steel material usage, exhibits higher stiffness and deformation capacity under the first mode shape loading. Conversely, the metastructure-coupled structure exhibits a more flexible behavior due to its structural configuration and reduced steel usage. The steel mass ratios of different cases are also highlighted by the colored points, with the range displayed in the color bar on the right. It is shown that the coupled structure efficiently reduces steel material usage compared to the optimized uncontrolled structure. In the case where no additional damping system is applied to the metastructures, i.e. considering an inherent damping of the metastructures equal to 0.02, a total of 11.3% of the steel mass can be saved. As the damping ratio ξ_{meta} of the metastructures increases, the optimization process entails lighter steel members. Nonetheless, Fig. 8 highlights that beyond 10% for ξ_{meta}, the α saturates around 77%, as the structural members reach the minimum permissible cross-sections required by standards for lateral stiffness and design stress limitations.

To appreciate the dynamic response of Case study 1, the case with ξ_{meta} = 0.05, also indicated in Table A.1 of the Appendix with ξ_{meta} = 0.05 was considered, where approximately 18% steel mass was saved. The transient deformation of the structure at the point of maximum

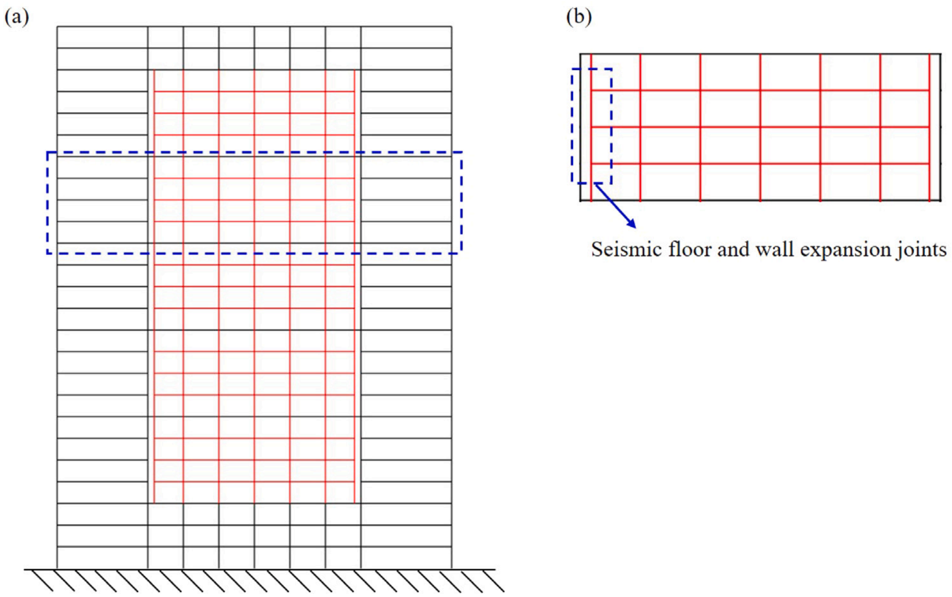

Fig. 7. Coupled MRF structure: (a) Lateral view; (b) Internal metastructure layout. (For interpretation of the references to color in this figure legend, the reader is referred to the web version of this article.)

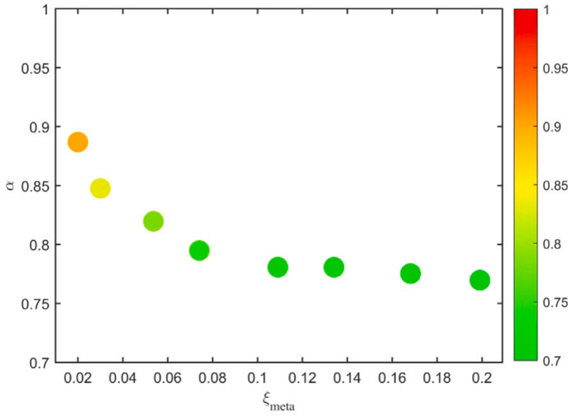

Fig. 8. Pareto front for the 25-story MRF structure. (For interpretation of the references to color in this figure legend, the reader is referred to the web version of this article.)

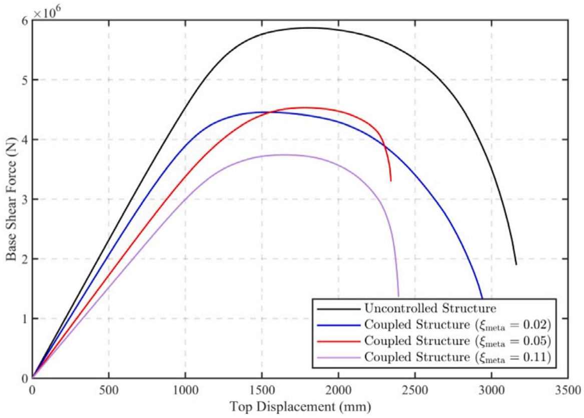

Fig. 9. Pushover results for MRF structures.

interstory drift, along with the yielding elements, is analyzed. The structural deformation of the uncontrolled structure is illustrated in Fig. 10(a), with yielding elements highlighted with red markers. For the IO limit state, yielding occurs at the outer-bay beam on the first story. Conversely, more extensive yielding is observed in the outer-bay and internal beams at the LS limit state. The maximum IDR values for the uncontrolled structure are provided in Fig. 10(c), where dashed and solid lines represent the IO and LS limit states, respectively. The largest IDR for the LS limit state is observed for the second story, i.e. 2.35%, which approaches the limit value of 2.5%; in addition, the maximum IDR for the IO limit state is 0.38% within the limit threshold of 0.7%.

With regard to the coupled structure, the interstory drift ratios have been controlled for both the columns of the outer frame structure and those of the internal metastructures. Maximum interstory drift values have been considered for the connected common stories between the metastructures and the outer frame structure. As shown in Fig. 11, for the hazard corresponding to the IO limit state, all elements remain in the elastic state, while yielding has occurred in both the metastructure and outer frame for the hazard relevant to the LS limit state. The maximum IDRs for the IO and LS limit states read 0.59% and 2.45%, respectively, both close to the limit values; this indicates an efficient performance of structural elements. The maximum relative displacement between the side columns of the metastructure and the outer frame inner columns is 53.7 mm, occurring at the 9th story.

The optimized results of the total mass including the steel frame and floor slab, as well as the dynamic characteristics of the metastructures and coupled system, are presented in the Table A.3. It can be found that the mass ratio of metastructures to the coupled structure is around 33% for MRFs. The relative displacement between the metastructure floors and the outer frame floors is summarized in the Table A.4. Among all scenarios, the largest relative displacement was observed as 73.7 mm, which remains within the motion allowance of the seismic expansion joints, in the range 0–175 mm.

4.2. Case study 2: a 20-story eccentrically braced steel frame

4.2.1. Building configuration

A steel eccentrically braced frame (EBF) building is selected for the second case study, following the configuration analyzed by Malhotra [51]. As shown in Fig. 12, the structure is designed with 6 equal

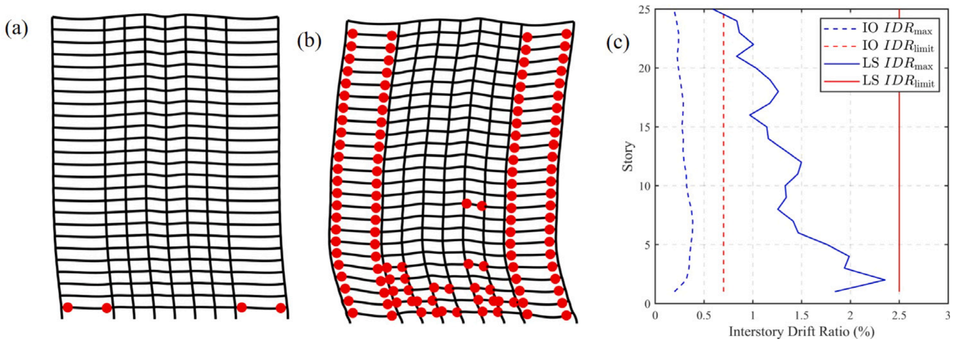

Fig. 10. Uncontrolled MRF structure results: (a) Maximum deformation for the hazard at the IO limit state; (b) Maximum deformation for the hazard at the LS limit state; (c) Distribution of maximum IDR values along the height.

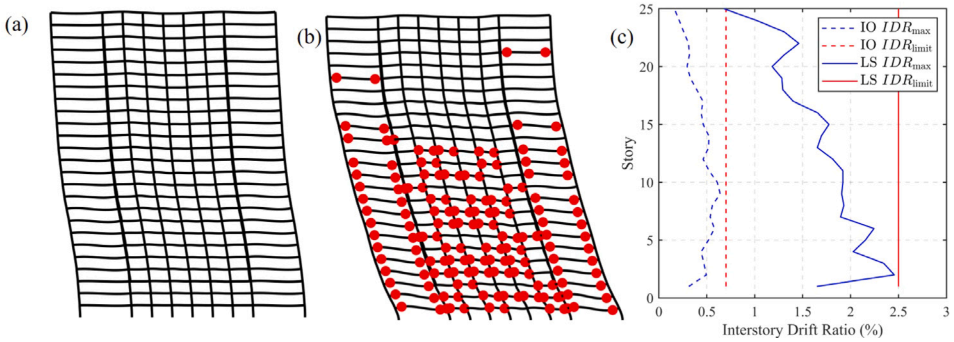

Fig. 11. Coupled MRF structure results: (a) Maximum deformation at the IO limit state; (b) Maximum deformation at the LS limit state; (c) Maximum IDR values for each story.

Table 3
Structural parameters of the EBF structure.

Bay length	4.57 m	Steel grade (ASTM A992)	f_{yk} = 345 MPa
Number of stories	20	Superimposed linear dead load	4 kN/m^2
Story height	3.66 m	Superimposed linear live load	2 kN/m^2

Table 4
Steel mass in the EBF structure with different ξ_{meta} values.

ξ_{meta}	Uncontrolled structure steel mass	Coupled structure steel mass	α
0.02	936.3	807.8	0.863
0.05		779.0	0.832
0.06		704.9	0.753
0.07		694.5	0.742
0.14		688.6	0.735
0.18		685.4	0.732

length 4.57 m bays, where eccentric braces and links are symmetrically placed in the two central bays. The link-beam length e is designed for shear yielding, ensuring that $e \leq 1.6M_p/V_p$, where M_p and V_p define the plastic moment and plastic shear capacities of the link, respectively. In braced bays, simple connections are used for beam-to-column joints, and the sections of the link elements are kept the same as those of the connected beams in the same bay. The detailed design parameters of the structure are listed in Table 3.

In the EBF coupled structure configuration, five three-story metastructures are periodically located, starting from the fourth story, as shown in red in Fig. 13. Similarly to the configuration of the MRF coupled structure, the periodic metastructures are connected to the main structure through braces and columns. The brace sections and beam-link lengths for both the metastructures and the outer frame are designed to be consistent in the vertical direction, ensuring a regular structural layout. The structure is designed according to the standards ANSI/AISC 341-16 [52], 360-16 [53], and ASCE/SEI 7-22 [46]. In the optimization process of the coupled EBF structure, the link-to-bay length ratio and the brace sections, as well as the metastructure damping ratio, beam and column sections are the variables to be optimized, and sections were selected from the American wide-flange (W) range. The links and their connected beams have been modeled in the “nonlinearBeamColumn” element of OpenSEES with three integration points, while the other structural elements used five integration points.

4.2.2. Optimization results

The limit values for IDR values corresponding to the IO and LS limit states were taken as 0.5% and 1.5%, respectively, in agreement with FEMA-356 [13]. The corresponding Pareto front results between steel mass reduction ratio α and metastructures' damping ratio ξ_{meta}, are provided in Fig. 14 and Table 4. The monotonic pushover results for the EBF uncontrolled structure and the coupled structures are shown in Fig. 15. As the inherent damping ratio of the metastructures increases, the coupled structure primarily dissipates energy through the internal metastructures, resulting in a lower peak base shear force. Similarly to the MRF, the EBF coupled structure also shows a remarkable weight reduction, especially when ξ_{meta} of the metastructure increases. For the case $\xi_{meta} = 0.02$, the coupled structure can already save up to 13.7% of the steel mass w.r.t. the uncontrolled structure. Additional results of both the EBF uncontrolled structure and the coupled structure where the internal metastructures have the basic $\xi_{meta} = 0.02$ are commented herein. Details of the designed sections and the mass ratio of the metastructures are given in Tables A.2 and A.3 of the Appendix, indicating that the locally resonant metastructures account for approximately 35% of the total mass. In addition, the dynamic characteristics of the metastructures and coupled structures in different scenarios are presented in Table A.5. As emphasized in Section 3, the proposed structure was not designed based on the tuned mass damper approach but rather through multi-objective optimization aligned with performance-based seismic design procedures, resulting in differences in their natural frequencies.

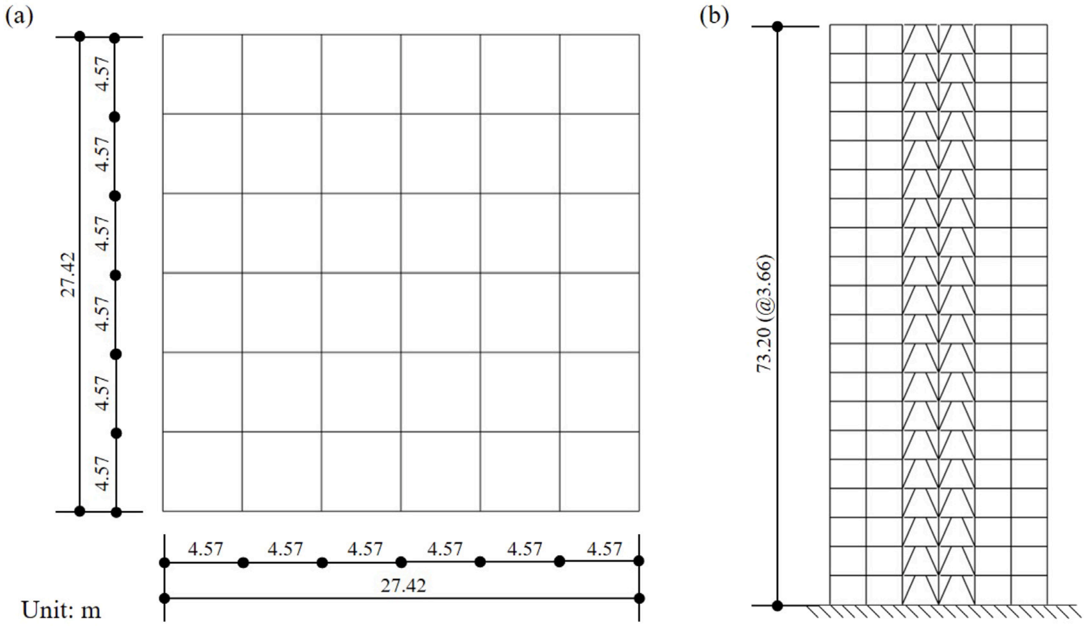

Fig. 12. Uncontrolled EBF structure: (a) Floor plan; (b) Lateral view.

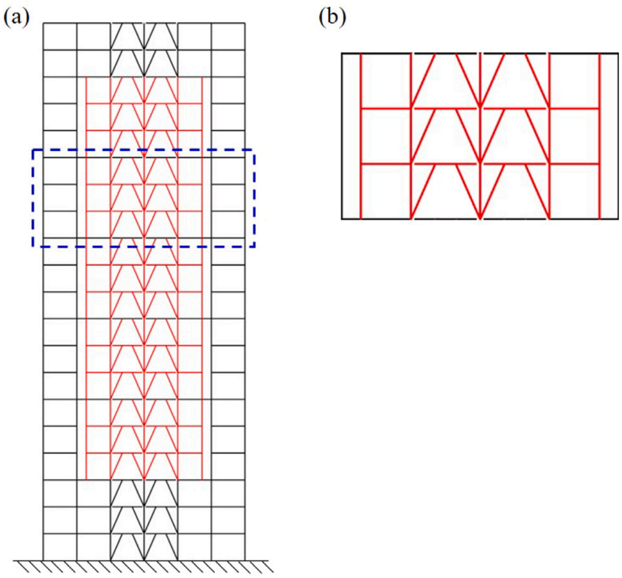

Fig. 13. Coupled EBF structure: (a) Lateral view; (b) Internal metastructure layout. (For interpretation of the references to color in this figure legend, the reader is referred to the web version of this article.)

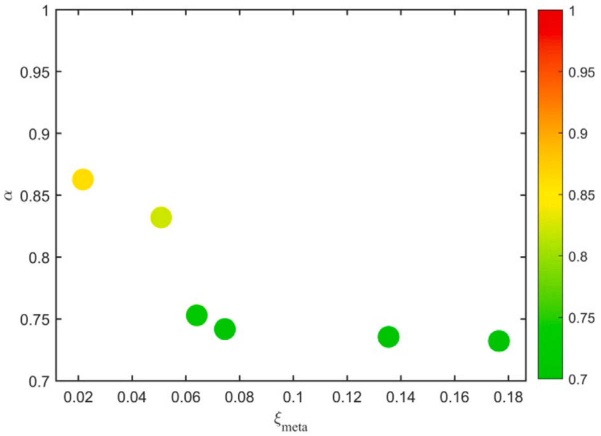

Fig. 14. Pareto front for the 20-story EBF structure. (For interpretation of the references to color in this figure legend, the reader is referred to the web version of this article.)

Fig. 16(a) and (b) present the deformation of the uncontrolled structure when the maximum drift occurs at the IO and LS limit states, respectively. No minor yielding can be found in the structure in the IO limit state, while yielding concentrates in the link and brace elements at the LS limit state; this damage pattern is foreseen in FEMA 356 standard for the bracing system. The structural interstory drifts in the two limit states are shown in Fig. 16(c), where maximum values approach 0.41% and 1.49%, i.e. safe values in agreement with the standards. The drift distribution for the EBF coupled structure, shown in Fig. 17(a) and (b), also exhibits a similar behavior at the IO limit state where no yielding has occurred. However, less yielding can be found in the links of the coupled structure at the LS design limit state. This is due to the marked mass reduction. According to the maximum IDR values depicted in Fig. 17(c), the interstory drifts for the coupled structure are below the thresholds for both limit states, indicating a favorable performance of the controlled system with a lightweight design.

5. Carbon emission assessment

The calculation of the CO2 equivalent in the life cycle, i.e. CO2e is crucial in sustainable construction, and it focus on total emissions from building materials throughout their life cycle. The decrease in operational carbon as a result of energy efficiency shifted the focus to reducing embodied CO2e, which is indeed vital to reduce GHG emissions of the construction sector and achieve sustainability targets [6,54,55]. Calculations of CO2e need a systematic assessment of carbon emissions – equivalent – stored throughout the entire life cycle of building materials and construction processes requiring a comprehensive Life Cycle Assessment (LCA) [56,57]. In 1997, the International Organization for Standards (ISO) published the ISO 14040 to establish the standard guideline for performing an LCA, which was later amended in 2006 and 2020 and published in the ISO 14044 [57,58].

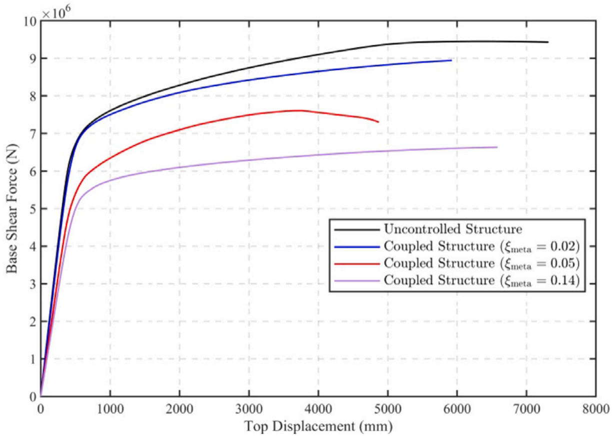

Fig. 15. Pushover results for EBF structures.

Table 5
Embodied carbon factors.

	Module A1-3 embodied carbon kgCO2e/kg	Module D embodied carbon kgCO2e/kg	Total embodied carbon kgCO2e/kg
ICE DB v3.0	1.550	−0.345	1.205
World Steel 2022	–	–	1.910
British Steel	2.450	−1.600	0.850
ArcelorMittal HSS	2.270	−1.320	0.950

Clearly, the first step is to collect data on the quantities of materials used, where each material and component has an associated embodied carbon factor, which represents the amount of carbon dioxide equivalent (CO2e) emissions per unit of that material. These factors are derived from databases or specific environmental product declarations (EPDs). Therefore, to obtain correct and accurate values is an essential part of performing an LCA and can be derived from several sources [59], including: EPDs [60]; industry data; government data; factors from commercial LCA databases (e.g., ICE database [61]); factors derived-aggregated from literature, and so on. Each data source varies in detail, specificity, and accuracy, depending on the region and application. Notably, the most accurate data can be obtained from EPDs, which their assessments are carried out by manufacturers.

Clearly, uncertainty regarding the accuracy of carbon factors is an important issue, with the use of EPDs for product-specific materials being the primary recommendation within the CEN standard for the sustainability of construction works [62]. However, there are valid arguments about the use of generic data as an accepted alternative due to unavailability. Issues and variations related to public procurement policies worldwide often mean that buildings are constructed with different materials that could vary than the EDP-available materials, thus reducing the precision of a product-specific LCA approach early in the procurement process. Finally, the use of generic data in a national context has been shown to have methodological validity and relevance [5,63].

Within the scope of this research, the focus is to optimize the weight of structural components, mainly the weight of the lateral resisting structural steel system, without altering the gravity-carrying structure, non-structural elements and maintaining acceptable reliability. As a result, the LCA has involved relevant structural components (beams and columns) with a comparative analysis of CO2e, to demonstrate the impact on life cycle carbon footprint (LCCF). For both case studies, the structural members and their weights for the optimized uncontrolled structure and the coupled structure configurations are summarized in Tables A.1 and A.2 in the Appendix. As mentioned, precise carbon factors are required for a reliable LCA; however, since the materials and sections considered in the case studies are generic elements, they are not associated with any specific manufacturer. Consequently, for a more accurate LCA, carbon factors from four different resources, namely: (i) Inventory of Carbon and Energy (ICE) Database v3.0 [61], (ii) World Steel Association's 2023 Sustainability Indicators report [64], EPDs of Structural Hollow Section by ArcelorMittal [65] and EPDs of British Steel for Steel sections [66] were considered; relevant values are presented in Table 5.

Based on the mass reduction results provided in Figs. 8 and 14, the corresponding reduction in CO2e is calculated according to Table 5, and presented in Tables 6–7 for the case studies, with the results also illustrated in Fig. 18. Notably, variations between emission databases lead to differences in the estimated CO2e reductions. The ICE Database provides estimates that are closer to the mean results, while the World Steel Database tends to overestimate the savings, indicating a higher CO2e per kilogram of steel. These discrepancies highlight the influence of database selection on the perceived effectiveness of the proposed structural designs. However, as depicted in Fig. 18, the overall trends and comparative benefits of the proposed approach remain consistent, with relative differences across scenarios being consistently maintained. Another important issue is the uncertainty arousing from the involvement of additional damping throughout the metastructures. Achieving a higher damping ratio not only leads to a more efficient use of materials but also significantly enhances CO2e savings, by reducing the overall environmental footprint. However, further increases in damping can be realized through the integration or installation of additional damping elements, such as braces, dampers, viscoelastic components, and other specialized systems. These enhancements provide greater flexibility in the optimization of the structural performance while maintaining environmental sustainability. Clearly, these elements come with a CO2e that can vary depending on many factors. However, no accurate information on approximate associated carbon factor, or publicly available EPDs could be found. In addition, the variety of available solutions and approaches introduces major uncertainty. Thus, the CO2e reduction values without additional damping devices were mainly considered; and the additional CO2e savings clearly depend on the associated CO2e values associated to damping systems. Finally, it can be remarked that the proposed design approach, without any additional damping device in the locally resonant metastructures, results in a reduction of 11.3% and 13.7% steel mass for the examined MRF and EBF buildings, respectively.

6. Conclusions and future perspectives

Design rules in structural codes, such as the Eurocodes and the ASCE, are highly generalized and simplified. In fact, the ease of use was one of the most important driver for their development. Moreover, apart from monetary optimization and societal risk acceptance with respect to life safety, they do not contain any account of objectives related to sustainability. Conversely, societal-risk approaches that include performance-based approaches and wave manipulation capabilities, facilitate a consistent way to identify reduced structural carbon footprint goals satisfying reliability. More specifically, coupled steel structures endowed with wave manipulation capabilities via finite locally resonant metamaterials, i.e. metastructures (LRMs), can be designed and optimized with the objectives of weight and subsequent carbon footprint reduction. In particular and to induce antiresonance, internal metastructures can be periodically distributed along the height of coupled (controlled) structures and vibrate in counterphase with the outer frame structures.

Along these lines, both the wave dispersion and attenuation properties of the proposed structural layout were analyzed in the frequency domain. Then, a design and multi-objective optimization procedure was developed for a coupled structure, targeting different seismic design limit states according to the performance-based seismic design methodology; in particular, hazards relevant to Immediate Occupancy (IO) and Life Safety (LS) were considered and controlled via interstory drifts. To

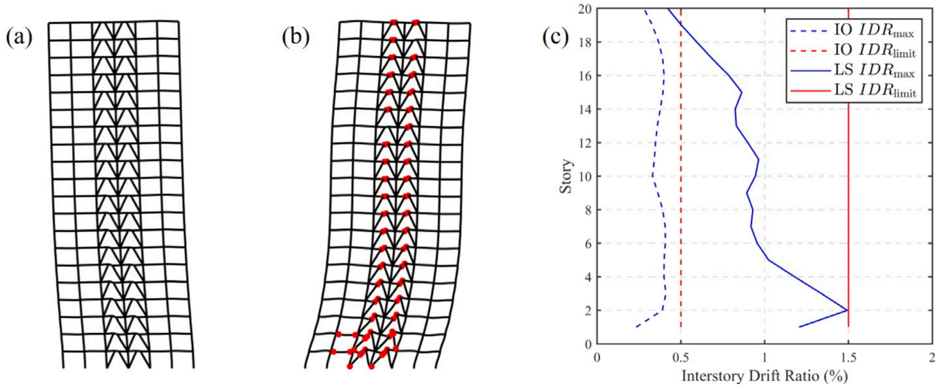

Fig. 16. Uncontrolled EBF structure results: (a) Maximum deformation for the hazard at the IO limit state; (b) Maximum deformation for the hazard at the LS limit state; (c) Distribution of maximum IDR values along the height.

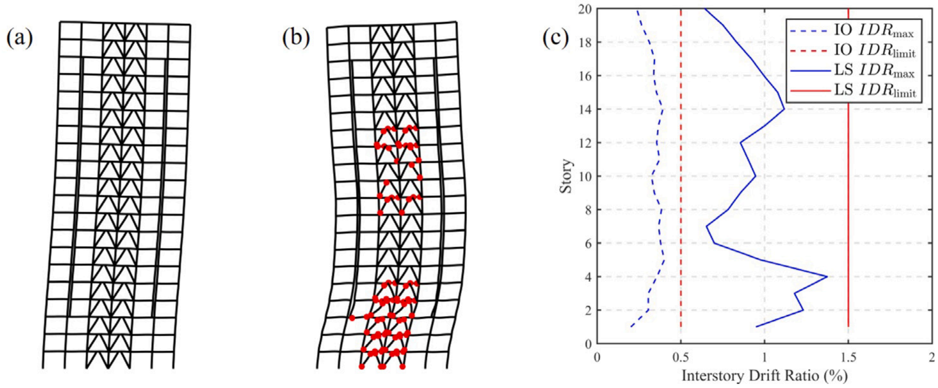

Fig. 17. Coupled EBF structure results: (a) Maximum deformation under IO limit state; (b) Maximum deformation under LS limit state; (c) Maximum IDR values for each story.

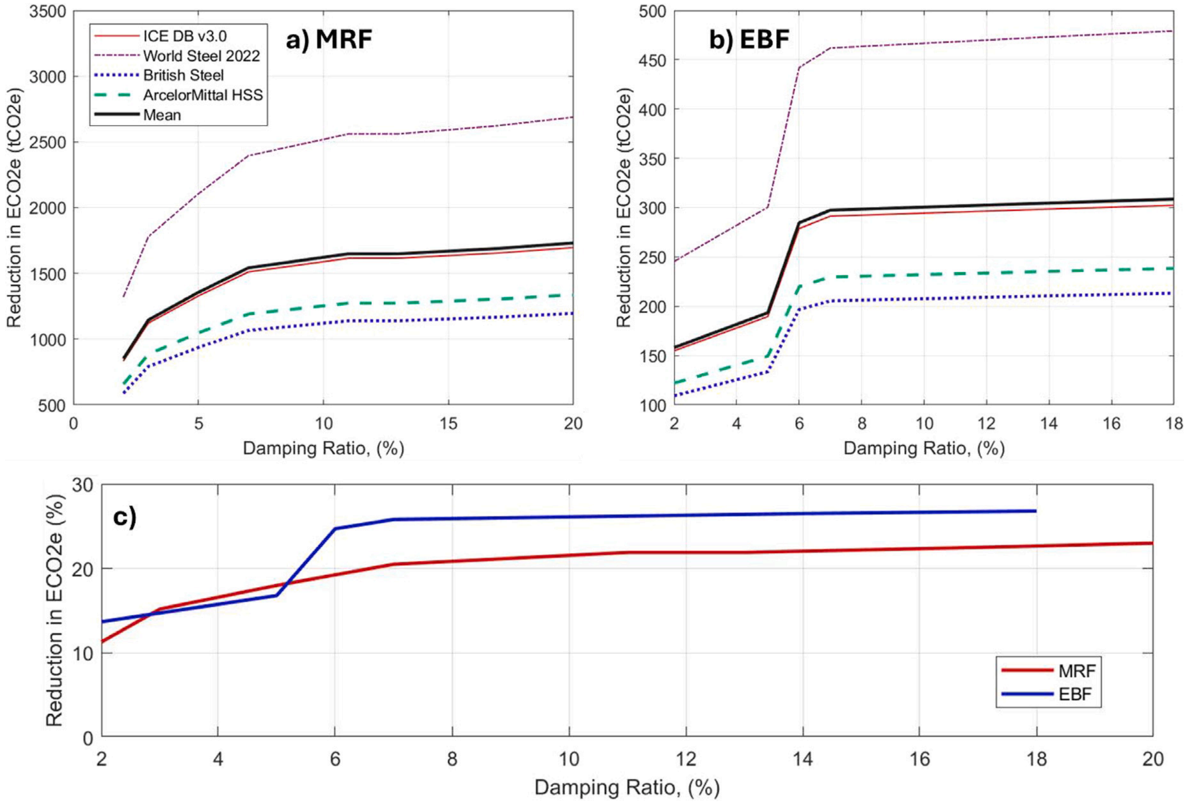

Fig. 18. Estimated embodied CO2e reduction values for (a) the MRF building, (b) the EBF building and (c) percentage of CO2e reduction w.r.t. the original layout vs. the metastructure damping ratio.

Table 6
Estimated CO2e reduction values for the Case Study 1: the 25-story MRF structure.

Damp. Ratio	Steel weight			Total embodied carbon reduction					
	Uncontrolled structure	Coupled structure	Reduction	ICE DB	WS 2022	BS	AM HSS	Mean	Ratio
	tons			tCO2e					%
0.02	6111.6	5420.3	−691.3	833.4	1320.4	587.6	656.8	849.6	11.3
0.03	6111.6	5180.3	−931.3	1122.7	1778.8	791.6	884.7	1144.4	15.2
0.05	6111.6	5009.3	−1102.3	1328.8	2105.4	937.0	1047.2	1354.6	18.0
0.07	6111.6	4857.7	−1253.9	1511.6	2395.0	1065.8	1191.2	1540.9	20.5
0.11	6111.6	4771.1	−1340.5	1616.0	2560.3	1139.4	1273.5	1647.3	21.9
0.13	6111.6	4771.0	−1340.6	1616.1	2560.6	1139.5	1273.6	1647.5	21.9
0.17	6111.6	4738.1	−1373.5	1655.7	2623.3	1167.4	1304.8	1687.8	22.5
0.20	6111.6	4704.0	−1407.6	1696.9	2688.5	1196.5	1337.2	1729.8	23.0

Table 7
Estimated CO2e reduction values for the Case Study 2: the 20-story EBF structure.

Damp. Ratio	Steel weight			Total embodied carbon reduction					
	Uncontrolled structure	Coupled structure	Reduction	ICE DB	WS 2022	BS	AM HSS	Mean	Ratio
	tons			tCO2e					%
0.02	936.3	807.8	−128.5	154.9	245.4	109.2	122.1	157.9	13.7
0.05	936.3	779.0	−157.3	189.6	300.4	133.7	149.4	193.3	16.8
0.06	936.3	704.9	−231.4	278.9	441.9	196.7	219.8	284.3	24.7
0.07	936.3	694.5	−241.8	291.5	461.8	205.5	229.7	297.1	25.8
0.14	936.3	688.6	−247.7	298.5	473.0	210.5	235.3	304.3	26.5
0.18	936.3	685.4	−250.8	302.4	479.1	213.2	238.3	308.2	26.8

evaluate the effectiveness of LRMs for optimum weight reduction, two case studies representing different steel frame layouts, i.e. a moment-resisting frame (MRF) and an eccentrically braced frame (EBF) were considered. In addition, the internal LRMs have been enhanced with proportional damping, to explore the trade-off between structural steel mass savings and the addition of passive damping systems. Successively, the weight of the coupled structures was optimized as a function of the damping in the metastructures. The mass savings and the subsequent embodied carbon reduction — approximatively ranged from 11.3% to 23.0% and 13.7% to 26.8%, for the MRF and EBF structures, respectively, depending on the metastructure damping values.

Future research requires to incorporate more innovative steel frame layouts, w.r.t. the 2D frame analyzed above; in these situations, the metastructure design could benefit from the selected tuning of mechanical properties inherent in LRMs. Clearly, irregular floor plans, complex architectural designs, and multi-directional seismic inputs, require more elaborated optimization schemes to be implemented, demanding more computational power. In alignment with the modular construction, further focus can be put on modularity of the metastructures together with standardization of designs, resulting in further reduction in material usage and CO2e. With more specific cases analyzed, a more comprehensive assessment of carbon emissions throughout the entire life cycle will be possible, including those associated with transportation and maintenance. These advancements would further enhance both the structural performance and sustainability of controlled systems.

CRediT authorship contribution statement

Jiawei Zhang: Writing – original draft, Investigation, Conceptualization. **Tugberk Guner:** Writing – original draft, Methodology. **Oreste S. Bursi:** Writing – review & editing, Funding acquisition, Conceptualization. **Zheng Lu:** Writing – review & editing, Supervision.

Declaration of competing interest

The authors declare that they have no known competing financial interests or personal relationships that could have appeared to influence the work reported in this paper.

Acknowledgments

The authors gratefully acknowledge the support from the China Scholarship Council (CSC), and the Italian Ministry of Education for the project DICAM-EXC (Departments of Excellence 2023–2027, grant L232/2016). Financial support from the National Natural Science Foundation of China (52178296) is highly appreciated. Finally, the third author acknowledges the National Project MUR PNRR M4C2-CN1-SPOKE 9.

Appendix

Owing to the symmetry of both the steel moment-resisting frame structure and eccentrically braced frame structure, only the cross-sections of half of the spans were selected during the optimization process. In particular, the steel element sections are labeled in Tables A.1 and A.2 based on their locations from left to right; for instance, Beam #n, where n represents the element's position. The beam and column elements of each internal metastructure are labeled with "meta" as a suffix. For the eccentrically braced frame systems, the length ratio of the link-beam to the bay length and the structural brace has also been considered as a parameter to be optimized. The detailed results for sections and damping ratios ξ_{meta} of both structural systems are presented in Tables A.1 and A.2, respectively. The eight and six optimized cases in the aforementioned tables correspond to the data presented in Fig. 8 and in Fig. 14, respectively.

The mass ratio is calculated as the total mass of all five metastructures divided by the total mass of the entire coupled structure, with results for MRF and EBF structures under varying metastructure inherent damping ratios summarized in Table A.3. The maximum relative displacements of the metastructure floors and outer frame floors for the coupled structures are provided in Table A.4. Table A.5 presents a comparison of the dynamic characteristics of the metastructure and the coupled structure, along with the connecting stiffness values for the metastructures.

Table A.1
Optimization results for the MRF structures.

Structural type	Total mass (tons)	ξ_{meta}	Beam#1	Beam#2	Beam#3	Beam#4	Column#1	Column#2	Column#3	Column#4	Column#5
Uncontrolled structure	6111.6	–	HE600 × 174	HE550A	HE800B	HE240M	TUBO500 × 500 × 25	TUBO500 × 500 × 30	TUBO400 × 400 × 22.2	TUBO500 × 500 × 40	TUBO340 × 340 × 25
Coupled structure #1	5420.3	0.02	HE600 × 151	HE700A	HE300B	HE700B	TUBO500 × 500 × 25	TUBO500 × 500 × 30	TUBO380 × 380 × 22.2	TUBO340 × 340 × 40	TUBO340 × 340 × 20
Coupled structure #2	5180.3	0.03	HE700 × 166	HE450M	HE700M	HE320B	TUBO500 × 500 × 25	TUBO500 × 500 × 30	TUBO340 × 340 × 20	TUBO360 × 360 × 28	TUBO340 × 340 × 20
Coupled structure #3	5009.3	0.05	HE700 × 166	HE700A	HE450A	HE400A	TUBO500 × 500 × 25	TUBO500 × 500 × 30	TUBO360 × 360 × 25	TUBO360 × 360 × 25	TUBO300 × 300 × 28
Coupled structure #4	4857.7	0.07	HE600 × 151	HE650B	HE450 × 123	HE360B	TUBO500 × 500 × 25	TUBO500 × 500 × 30	TUBO400 × 400 × 22.2	TUBO320 × 320 × 22.2	TUBO340 × 340 × 28
Coupled structure #5	4771.1	0.11	HE600 × 151	HE600 × 151	HE600A	HE450A	TUBO500 × 500 × 25	TUBO500 × 500 × 30	TUBO380 × 380 × 20	TUBO400 × 400 × 22.2	TUBO340 × 340 × 20
Coupled structure #6	4771.0	0.13	HE700 × 166	HE600 × 151	HE400A	HE450 × 123	TUBO500 × 500 × 25	TUBO500 × 500 × 30	TUBO380 × 380 × 22.2	TUBO380 × 380 × 25	TUBO360 × 360 × 22.2
Coupled structure #7	4738.1	0.17	HE600 × 151	HE700 × 166	HE600A	HE450 × 123	TUBO500 × 500 × 25	TUBO500 × 500 × 30	TUBO360 × 360 × 25	TUBO340 × 340 × 25	TUBO360 × 360 × 20
Coupled structure #8	4704.0	0.20	HE600 × 151	HE650A	HE600A	HE300B	TUBO500 × 500 × 25	TUBO500 × 500 × 30	TUBO320 × 320 × 25	TUBO340 × 340 × 25	TUBO360 × 360 × 20

Structural type	Total mass (tons)	ξ_{meta}	Beam$_{\text{meta}}$ #1	Beam$_{\text{meta}}$ #2	Beam$_{\text{meta}}$ #3	Column$_{\text{meta}}$ #1	Column$_{\text{meta}}$ #2	Column$_{\text{meta}}$ #3	Column$_{\text{meta}}$ #4
Uncontrolled structure	6111.6	–	–	–	–	–	–	–	
Coupled structure #1	5420.3	0.02	HE450 × 123	HE700A	HE280M	TUBO400 × 400 × 30	TUBO500 × 500 × 25	TUBO360 × 360 × 20	TUBO340 × 340 × 17.5
Coupled structure #2	5180.3	0.03	HE450 × 123	HE700 × 166	HE700 × 166	TUBO140 × 140 × 14.2	TUBO340 × 340 × 17.5	TUBO500 × 500 × 25	TUBO300 × 300 × 20
Coupled structure #3	5009.3	0.05	HE400M	HE400 × 107	HE300A	TUBO240 × 240 × 12.5	TUBO500 × 500 × 25	TUBO380 × 380 × 20	TUBO340 × 340 × 20
Coupled structure #4	4857.7	0.07	HE320A	HE700A	HE200M	TUBO280 × 280 × 16	TUBO500 × 500 × 25	TUBO340 × 340 × 17.5	TUBO360 × 360 × 20
Coupled structure #5	4771.1	0.11	HE180M	HE650A	HE450A	TUBO140 × 140 × 10	TUBO340 × 340 × 25	TUBO450 × 450 × 25	TUBO320 × 320 × 17.5
Coupled structure #6	4771.0	0.13	HE600 × 137	HE360A	HE450 × 123	TUBO260 × 260 × 16	TUBO450 × 450 × 25	TUBO340 × 340 × 20	TUBO320 × 320 × 22.2
Coupled structure #7	4738.1	0.17	HE360A	HE600A	HE300B	TUBO200 × 200 × 12.5	TUBO380 × 380 × 28	TUBO380 × 380 × 22.2	TUBO320 × 320 × 20
Coupled structure #8	4704.0	0.20	HE360A	HE500A	HE600 × 137	TUBO180 × 180 × 14.2	TUBO380 × 380 × 20	TUBO400 × 400 × 22.2	TUBO340 × 340 × 20

Table A.2
Optimization results for the EBF structures.

Structural type	Total mass (tons)	ξ_{meta}	Beam #1	Beam #2	Beam #3	Column #1	Column #2	Column #3	Column #4
Uncontrolled structure	936.3	–	W21 × 44	W33 × 118	W12 × 44	W12 × 58	W24 × 146	W12 × 96	W14 × 48
Coupled structure #1	807.8	0.02	W24 × 55	W33 × 118	W14 × 61	W12 × 58	W40 × 211	W21 × 111	W12 × 58
Coupled structure #2	779.0	0.05	W12 × 19	W24 × 62	W21 × 57	W12 × 50	W30 × 173	W24 × 131	W14 × 74
Coupled structure #3	704.9	0.06	W12 × 22	W24 × 62	W24 × 62	W12 × 45	W33 × 354	W21 × 122	W10 × 39
Coupled structure #4	694.5	0.07	W14 × 26	W18 × 35	W30 × 90	W12 × 50	W33 × 201	W24 × 131	W10 × 45
Coupled structure #5	688.6	0.14	W6 × 16	W30 × 124	W18 × 40	W21 × 73	W30 × 191	W24 × 131	W10 × 39
Coupled structure #6	685.4	0.18	W12 × 22	W16 × 50	W18 × 60	W12 × 45	W40 × 277	W12 × 96	W27 × 129

Structural type	Total mass (tons)	ξ_{meta}	Beam$_{\text{meta}}$ #1	Beam$_{\text{meta}}$ #2	Column$_{\text{meta}}$ #1	Column$_{\text{meta}}$ #2	Column$_{\text{meta}}$ #3	Brace	Link length ratio
Uncontrolled structure	936.3	–	–	–	–	–	–	W10 × 49	0.1055
Coupled structure #1	807.8	0.02	W33 × 152	W18 × 40	W16 × 67	W21 × 101	W24 × 68	W10 × 39	0.1039
Coupled structure #2	779.0	0.05	W30 × 124	W27 × 84	W16 × 77	W21 × 111	W10 × 100	W18 × 60	0.1162
Coupled structure #3	704.9	0.06	W24 × 55	W24 × 68	W21 × 62	W21 × 101	W14 × 43	W12 × 50	0.2057
Coupled structure #4	694.5	0.07	W24 × 62	W21 × 50	W24 × 76	W24 × 117	W12 × 40	W16 × 50	0.1244
Coupled structure #5	688.6	0.14	W24 × 68	W24 × 62	W18 × 86	W21 × 111	W8 × 28	W8 × 31	0.1287
Coupled structure #6	685.4	0.18	W21 × 101	W18 × 35	W24 × 76	W21 × 101	W18 × 60	W10 × 45	0.1680

Table A.3
Mass ratio of the metastructure over the coupled structure.

Structural type	ξ_{meta}	Metastructure total mass (t)	Coupled structure total mass (t)	Mass ratio (%)
MRF structure	0.02	23 561.60	70 094.25	33.61
	0.03	22 792.95	69 824.25	32.64
	0.05	22 951.71	69 641.73	32.96
	0.07	22 881.83	69 461.28	32.94
	0.11	22 762.44	69 386.04	32.81
	0.13	22 742.24	69 353.10	32.79
	0.17	22 705.79	69 341.76	32.74
	0.20	22 633.16	69 295.14	32.66
EBF structure	0.02	2775.17	7969.36	34.82
	0.05	2898.27	7935.76	36.52
	0.06	2730.34	7849.31	34.78
	0.07	2763.90	7837.22	35.27
	0.14	2708.55	7830.34	34.59
	0.18	2750.73	7826.21	35.15

Table A.4
Relative displacement between metastructure floors and outer frame floors.

Structural type	ξ_{meta}	Relative displacement (mm)
MRF structure	0.02	73.7
	0.03	71.3
	0.05	53.7
	0.07	40.0
	0.11	18.7
	0.13	57.0
	0.17	45.0
	0.20	44.6
EBF structure	0.02	17.2
	0.05	28.1
	0.06	14.3
	0.07	17.2
	0.14	11.8
	0.18	12.8

Table A.5

Dynamic characteristics of the uncontrolled structures and coupled structures.

Structural type	ξ_{meta}	Metastructure connecting stiffness (10^3 kN/m)	Metastructure frequency (Hz)	Structural first threes frequencies (Hz)
MRF uncontrolled structure	–	–	–	0.16, 0.49, 0.87
MRF coupled structure	0.02	109.17	3.25	0.16, 0.48, 0.83
	0.03	81.21	2.85	0.15, 0.47, 0.81
	0.05	85.25	2.91	0.15, 0.46, 0.80
	0.07	80.39	2.83	0.14, 0.43, 0.75
	0.11	63.91	2.53	0.14, 0.43, 0.73
	0.13	70.06	2.65	0.14, 0.44, 0.75
	0.17	59.78	2.45	0.14, 0.43, 0.72
	0.20	60.57	2.47	0.14, 0.43, 0.73
EBF uncontrolled structure	–	–	–	0.82, 2.71, 4.46
EBF coupled structure	0.02	468.92	17.31	0.81, 2.61, 4.90
	0.05	676.64	20.35	0.75, 2.51, 4.74
	0.06	456.72	17.22	0.71, 2.26, 4.20
	0.07	554.63	18.86	0.71, 2.28, 4.30
	0.14	385.50	15.89	0.69, 2.27, 4.23
	0.18	458.90	17.20	0.69, 2.18, 4.08

Data availability

Data will be made available on request.

References

[1] United Nations Environment Programme. 2022 global status report for buildings and construction. 2022.

[2] European Commission. Buildings and construction. 2024, URL https://single-market-economy.ec.europa.eu/industry/sustainability/buildings-and-construction_en.

[3] Chen W, Yang S, Zhang X, Jordan ND, Huang J. Embodied energy and carbon emissions of building materials in China. Build Environ 2022;207:108434. http://dx.doi.org/10.1016/j.buildenv.2021.108434.

[4] Ramesh T, Prakash R, Shukla KK. Life cycle energy analysis of buildings: An overview. Energy Build 2010;42(10):1592–600. http://dx.doi.org/10.1016/j.enbuild.2010.05.007.

[5] Pomponi F, De Wolf C, Moncaster A. Embodied carbon in buildings. Springer Int Publ AG 2018;20:443–60.

[6] Akbarnezhad A, Xiao J. Estimation and minimization of embodied carbon of buildings: A review. Build 2017;7(1):5. http://dx.doi.org/10.3390/buildings7010005.

[7] Rafiq Y, Beck M. A decision support tool for multi-disciplinary conceptual design. Struct Eng 2008;86(1):37–42.

[8] Hingorani R, Köhler J. Towards optimised decisions for resource and carbon-efficient structural design. Civ Eng Environ Syst 2023;40(1–2):1–31. http://dx.doi.org/10.1080/10286608.2023.2198767.

[9] Kanyilmaz A, Tichell PRN, Loiacono D. A genetic algorithm tool for conceptual structural design with cost and embodied carbon optimization. Eng Appl Artif Intell 2022;112:104711. http://dx.doi.org/10.1016/j.engappai.2022.104711.

[10] Kanyilmaz A, Hoi Dang V, Kondratenko A. How does conceptual design impact the cost and carbon footprint of structures? Struct 2023;58:105102. http://dx.doi.org/10.1016/j.istruc.2023.105102.

[11] Deb K, Pratap A, Agarwal S, Meyarivan T. A fast and elitist multiobjective genetic algorithm: NSGA-II. IEEE Trans Evol Comput 2002;6(2):182–97. http://dx.doi.org/10.1109/4235.996017.

[12] Linkov I, Trump BD. The science and practice of resilience. Springer; 2019.

[13] Federal Emergency Management Agency. FEMA 356: Prestandard and commentary for the seismic rehabilitation of buildings. Tech. rep. FEMA 356, Washington, D.C.: Federal Emergency Management Agency; 2000.

[14] Park HS, Hwang JW, Oh BK. Integrated analysis model for assessing CO_2 emissions, seismic performance, and costs of buildings through performance-based optimal seismic design with sustainability. Energy Build 2018;158:761–75. http://dx.doi.org/10.1016/j.enbuild.2017.10.070.

[15] Hasik V, Chhabra JP, Warn GP, Bilec MM. Review of approaches for integrating loss estimation and life cycle assessment to assess impacts of seismic building damage and repair. Eng Struct 2018;175:123–37. http://dx.doi.org/10.1016/j.engstruct.2018.08.011.

[16] Mergos PE. Seismic design of reinforced concrete frames for minimum embodied CO2 emissions. Energy Build 2018;162:177–86. http://dx.doi.org/10.1016/j.enbuild.2017.12.039.

[17] Del Vecchio C, Di Ludovico M, Prota A, Manfredi G. Analytical model and design approach for FRP strengthening of non-conforming RC corner beam–column joints. Eng Struct 2015;87:8–20. http://dx.doi.org/10.1016/j.engstruct.2015.01.013.

[18] Tsonos A-DG. Performance enhancement of R/C building columns and beam–column joints through shotcrete jacketing. Eng Struct 2010;32(3):726–40. http://dx.doi.org/10.1016/j.engstruct.2009.12.001.

[19] Calvi G. Choices and criteria for seismic strengthening. J Earthq Eng 2013;17(6):769–802. http://dx.doi.org/10.1080/13632469.2013.781556.

[20] Ferraioli M, Mandara A. Base isolation for seismic retrofitting of a multiple building structure: Design, construction, and assessment. Math Probl Eng 2017;2017(1):4645834. http://dx.doi.org/10.1155/2017/4645834.

[21] Matta E. Lifecycle cost optimization of tuned mass dampers for the seismic improvement of inelastic structures. Earthq Eng Struct Dyn 2018;47(3):714–37. http://dx.doi.org/10.1002/eqe.2987.

[22] Akhlagh Pasand A, Zahrai SM. Seismic control of tall buildings using vertically distributed multiple tuned mass dampers. Struct Des Tall Spec Build 2024;33(14):e2123. http://dx.doi.org/10.1002/tal.2123.

[23] Chen Z, Wang G, Lim C. Artificially engineered metaconcrete with wide bandgap for seismic surface wave manipulation. Eng Struct 2023;276:115375. http://dx.doi.org/10.1016/j.engstruct.2022.115375.

[24] Hao S, Sheng H, Lyu X, Ding Q. A novel locally resonant metastructure with soft-material rings for broadband and low frequency vibration attenuation. Eng Struct 2022;272:114978. http://dx.doi.org/10.1016/j.engstruct.2022.114978.

[25] Bursi OS, Basone F, Wenzel M. Stochastic analysis of locally resonant linear and hysteretic metamaterials for seismic isolation of process equipment. J Sound Vib 2021;510:116263. http://dx.doi.org/10.1016/j.jsv.2021.116263.

[26] Xiao L, Sun F, Bursi OS, Li H, Wang M. Experimental study on the seismic mitigation performance of metafoundations on a uniform soil layer. J Earthq Eng 2023;27(14):4206–36. http://dx.doi.org/10.1080/13632469.2022.2162632.

[27] Guner T, Bursi OS, Erlicher S. Optimization and performance of metafoundations for seismic isolation of small modular reactors. Comput-Aided Civ Infrastruct Eng 2022;38(12):1558–82. http://dx.doi.org/10.1111/mice.12902.

[28] Xia Y, Ruzzene M, Erturk A. Dramatic bandwidth enhancement in nonlinear metastructures via bistable attachments. Appl Phys Lett 2019;114(9).

[29] Zhao T, Yang Z, Tian W. Tunable nonlinear metastructure with periodic bi-linear oscillators for broadband vibration suppression. Thin-Walled Struct 2023;191:110975. http://dx.doi.org/10.1016/j.tws.2023.110975.

[30] Kalderon M, Mantakas A, Paradeisiotis A, Antoniadis I, Sapountzakis EJ. Locally resonant metamaterials utilizing dynamic directional amplification: An application for seismic mitigation. Appl Math Model 2022;110:1–16. http://dx.doi.org/10.1016/j.apm.2022.05.037.

[31] Guner T, Bursi OS, Broccardo M. Seismic vibration mitigation of steel storage tanks by metafoundations endowed with linear and bistable columns. Bull Earthq Eng 2024;22(1):29–54. http://dx.doi.org/10.1007/s10518-023-01692-0.

[32] Sun F, Xiao L. Bandgap characteristics and seismic applications of inerter-in-lattice metamaterials. J Eng Mech 2019;145(9):04019067. http://dx.doi.org/10.1061/(ASCE)EM.1943-7889.0001642.

[33] Xia Y, Erturk A, Ruzzene M. Topological edge states in quasiperiodic locally resonant metastructures. Phys Rev Appl 2020;13:014023. http://dx.doi.org/10.1103/PhysRevApplied.13.014023.

[34] Hussein MI, Frazier MJ. Metadamping: An emergent phenomenon in dissipative metamaterials. J Sound Vib 2013;332(20):4767–74. http://dx.doi.org/10.1016/j.jsv.2013.04.041.

[35] Van Belle L, Claeys C, Deckers E, Desmet W. On the impact of damping on the dispersion curves of a locally resonant metamaterial: Modelling and experimental validation. J Sound Vib 2017;409:1–23. http://dx.doi.org/10.1016/j.jsv.2017.07.045.

[36] Chopra A. Dynamics of structures, theory and applications to earthquake engineering. Prentice-hall international series in civil engineering and engineering mechanics, Pearson Education; 2007.

[37] McKenna F. Object oriented finite element analysis: Frameworks for analysis algorithms and parallel computing (Ph.D. diss.), Berkeley: University of California; 1997.

[38] Colajanni P, Ahmed M, Pagnotta S, Orlando P. A review of friction dissipative beam-to-column connections for the seismic design of MRFs. Appl Sci 2024;14(6). http://dx.doi.org/10.3390/app14062291.

[39] Losanno D, Spizzuoco M, Serino G. An optimal design procedure for a simple frame equipped with elastic-deformable dissipative braces. Eng Struct 2015;101:677–97. http://dx.doi.org/10.1016/j.engstruct.2015.07.055.

[40] Aied Qissab Al-Janabi M, Topkaya C. Seismic performance of eccentrically braced frames designed to AISC341 and EC8 specifications. Struct 2021;29:339–59. http://dx.doi.org/10.1016/j.istruc.2020.11.031.

[41] Filippou FC, Popov EP, Bertero VV. Effects of bond deterioration on hysteretic behavior of reinforced concrete joints. Earthquake Engineering Research Center, University of California, Berkeley; 1983.

[42] Bu H, He L, Jiang H. Seismic fragility assessment of steel frame structures equipped with steel slit shear walls. Eng Struct 2021;249:113328. http://dx.doi.org/10.1016/j.engstruct.2021.113328.

[43] Carreño R, Lotfizadeh KH, Conte JP, Restrepo JI. Material model parameters for the Giuffrè-Menegotto-Pinto uniaxial steel stress-strain model. J Struct Eng 2020;146(2):04019205. http://dx.doi.org/10.1061/(ASCE)ST.1943-541X.0002505.

[44] Castaneda N, Gao X, Dyke SJ. Computational tool for real-time hybrid simulation of seismically excited steel frame structures. J Comput Civ Eng 2015;29(3):04014049. http://dx.doi.org/10.1061/(ASCE)CP.1943-5487.0000341.

[45] Ministero delle Infrastrutture e dei Trasporti. NTC 2018: Norme tecniche per le costruzioni. Rome, Italy: Gazzetta Ufficiale della Repubblica Italiana; 2018, no. D.M. 17/01/2018, In Italia.

[46] American Institute of Steel Construction. ASCE/SEI 7-22: Minimum design loads and associated criteria for buildings and other structures. Reston, VA, USA: American Society of Civil Engineers; 2022.

[47] Hori Y, Suzuki Y, Kolozvari K, Johansson O, Naeim F, Nakashima M. A comparative study of seismic analysis, design, and collapse safety margins of tall buildings in the United States and Japan, part I: Performance-based analysis and design. Earthq Spectra 2022;38(3):2297–318. http://dx.doi.org/10.1177/87552930221076528.

[48] European Committee for Standardization. EN 1993: Eurocode 3: Design of steel structures, part 1-1: General rules and rules for buildings. EN 1993, Brussels, Belgium: European Committee for Standardization (CEN); 2005.

[49] European Committee for Standardization. EN 1998: Eurocode 8: Design of structures for earthquake resistance. part 1: General rules, seismic actions and rules for buildings. EN 1998, Brussels, Belgium: European Committee for Standardization (CEN); 2004.

[50] Otsuki Y, Kurata M, Skalomenos KA, Ikeda Y. Damage sequence and safety margin assessment of expansion joints by shake table testing. Earthq Eng Struct Dyn 2019;48(1):3–26. http://dx.doi.org/10.1002/eqe.3120.

[51] Malhotra PK. Designing to the strongest ground motions. American Society of Civil Engineers; 2023, http://dx.doi.org/10.1061/9780784485194.

[52] American Institute of Steel Construction. ANSI/AISC 341-16: Seismic provisions for structural steel buildings. Chicago, IL, USA: American Institute of Steel Construction; 2016.

[53] American Institute of Steel Construction. ANSI/AISC 360-16: Specification for structural steel buildings. Chicago, IL, USA: American Institute of Steel Construction; 2016.

[54] Dixit MK, Fernández-Solís JL, Lavy S, Culp CH. Identification of parameters for embodied energy measurement: A literature review. Energy Build 2010;42(8):1238–47. http://dx.doi.org/10.1016/j.enbuild.2010.02.016.

[55] Ibn-Mohammed T, Greenough R, Taylor S, Ozawa-Meida L, Acquaye A. Operational vs. embodied emissions in buildings—A review of current trends. Energy Build 2013;66:232–45. http://dx.doi.org/10.1016/j.enbuild.2013.07.026.

[56] Pomponi F, Giesekam J, Hart J, D'Amico B. Embodied carbon: status quo and suggested roadmap. 2020.

[57] International Organization for Standardization. ISO 14040:1997 environmental management—Life cycle assessment—Principles and framework. Geneva, Switzerland: International Organization for Standardization; 1997.

[58] International Organization for Standardization. Environmental management—Life cycle assessment—Requirements and guidelines. ISO 14044. Geneva, Switzerland: International Organization for Standardization; 2006.

[59] Mohebbi G, Bahadori-Jahromi A, Ferri M, Mylona A. The role of embodied carbon databases in the accuracy of life cycle assessment (LCA) calculations for the embodied carbon of buildings. Sustain 2021;13(14):7988. http://dx.doi.org/10.3390/su13147988.

[60] Butcher K. Embodied carbon in building services—A calculation methodology—CIBSE TM 65. London, UK: Chartered Institution of Building Services Engineers; 2021.

[61] Hammond G, Jones C. Inventory of carbon and energy (ICE) database v3.0. 2019, URL https://circularecology.com/embodied-carbon-footprint-database.html [Accessed 05 October 2024].

[62] für Normung e.V. (DIN) DI. Sustainability of construction works – Assessment of environmental performance of buildings – Calculation method (German Version EN 15978:2011). Berlin, Germany: Beuth Verlag; 2012, EN 15978:2012.

[63] Silvestre JD, Lasvaux S, Hodková J, de Brito J, Pinheiro MD. Nativelca-a systematic approach for the selection of environmental datasets as generic data: application to construction products in a national context. Int J Life Cycle Assess 2015;20:731–50. http://dx.doi.org/10.1007/s11367-015-0885-8.

[64] Association WS. Sustainability indicators 2023 report. 2023, URL worldsteel.org/steel-topics/sustainability/sustainability-indicators-2023-report/ [Accessed 05 October 2024].

[65] Europe ATP. Environmental product declaration: Structural hollow section. 2020, URL https://epd-online.com, EPD-ARC-20190180-CBD1-EN, PDF Document.

[66] Steel B. Environmental product declaration: Steel rails and sections (including semi-finished long products). 2020, URL https://www.britishsteel.co.uk, EPD-TS-2020-003, PDF Document.